Direct numerical simulation of VHF radar measurements of turbulence in the mesosphere

Dorothy Gibson-Wilde, Joseph Werne, and David Fritts
Colorado Research Associates, Boulder

Reginald Hill
NOAA Environmental Technology Laboratory, Boulder, Colorado

Abstract

We simulate very high frequency (VHF) radar backscatter from turbulent irregularities in the mesosphere and examine the process of calculating key turbulence parameters from radar Doppler spectral moments. Mesospheric turbulence is represented by a three-dimensional (3-D) direct numerical simulation (DNS) of a turbulent layer generated by Kelvin–Helmholtz instability, which exhibits inertial range turbulence characteristics. A subgrid-scale turbulence advection model is used to parameterize the unresolved small-scale structure of mesospheric temperature, ion species, and electron mixing ratios and to derive the radar backscatter cross sections. Energy and thermal dissipation rates are calculated from the 3-D velocity and temperature derivatives of the DNS. Doppler spectral widths relevant to various mesospheric radar observations are then determined from explicit calculation of spectral moments. We then present a comparison between the turbulence parameters calculated from the DNS and those calculated from the Doppler spectral moments.

1. Introduction

Turbulence in the mesosphere (~50–90 km altitude) can be generated by a variety of dynamical and convective instability processes. Here we examine the detailed structure of a turbulent layer resulting from the breakdown of a Kelvin–Helmholtz (KH) dynamical shear instability. *Røyrvik* [1983] and *Røyrvik and Smith* [1984] suggested the existence of large-scale vortices in the mesosphere, supported by vertical velocity observations, and interpreted these as KH vortices. Vortex horizontal extents of ~600 m were estimated from total phase shifts [*Røyrvik,* 1983]. Numerical modeling studies of gravity wave breaking and the onset of turbulence have exhibited a primary convective instability and a subsequent dynamical shear instability at lower heights [*Fritts et al.,* 1994, 1997; *Liu et al.,* 1999]. Observations and modeling of noctilucent cloud structures at mesopause heights have suggested large-scale bands resulting from gravity wave breaking, accompanied by smaller-scale (horizontal scale ~3–10 km) "billow structures" (i.e., vortex tubes) oriented orthogonally to the large-scale bands [*Thomas,* 1991; *Fritts et al.,* 1993]. "Ripple structures" (horizontal scale ~5–10 km) present in hydroxyl (OH) airglow observations [*Taylor and Hapgood,* 1990] have been interpreted as wave-breaking signatures with the aid of simultaneous wind and temperature observations [*Hecht et al.,* 1997; *Fritts et al.,* 1997].

Turbulent momentum fluxes alter mean winds, temperatures, and also atmospheric constituent distributions. Realization of the importance of turbulence generation and evolution in the mesosphere has led us to the application of a direct numerical simulation (DNS) of a turbulent layer. No measurement technique is able to fully characterize the dynamical, chemical, and ionization processes in this region at turbulent scales; hence numerical simulation is the only approach to quantitative investigation of turbulent structures in the mesosphere and to testing the extraction of turbulence parameters from radar observations.

Mesosphere–stratosphere–troposphere (MST) radars at very high frequency (VHF, 30–300 MHz) and ultrahigh frequency (UHF, 0.3–3 GHz) have provided extensive wind velocity measurements in the mesosphere [e.g., *Balsley and Gage,* 1980]. Key MST radar measurements that determine mesospheric dynamical variability are the backscattered power or signal–to–noise ratio (SNR), the Doppler velocity, and the width of the Doppler spectrum. Doppler velocity obtained using a vertical beam is often interpreted as an atmospheric vertical velocity, although this interpretation is not always justified. Doppler spectral width is related to the root–mean–square (RMS) velocity perturbations and is associated with the occurrence of turbulent regions [e.g., *Gage et al.,* 1980; *Hocking,* 1983]. However, effects such as beam broadening and shear broadening may give rise to spurious increases in observed Doppler spectral width [*Hocking,* 1983]. The interpretation of these Doppler spectral moments is investigated in depth in this study.

Medium frequency (MF, 0.3–3 MHz) radars provide horizontal wind velocity measurements in the mesosphere with typical height resolutions of 2–4 km. This height resolution is insufficient to resolve small-scale features in the mesosphere; however, spectral-based techniques have been suggested for the extraction of turbulence parameters from MF radar observations [e.g., *Hocking,* 1983, 1985].

Rocket-borne measurements provide ion and electron number densities, as well as temperature and wind measurements, in the mesosphere with high vertical resolution. *Røyrvik and Smith* [1984], *Ulwick et al.* [1988], *Watkins et al.* [1988], *Inhester et al.* [1990], and *Kelley et al.* [1990] have addressed the issue of comparison between rocket and VHF radar observations of turbulent regions in the mesosphere. Using the Jicamarca, Peru, VHF radar, *Røyrvik and Smith* [1984] found agreement between radar backscattered power and a scattering cross section determined from rocket-measured electron concentrations. They attributed irregularities in refractive index to a layer of isotropic turbulence in the neutral atmosphere. *Watkins et al.* [1988] obtained independent estimates of energy dissipation rates from rocket and radar observations during the Structure and Atmospheric Turbulence Environment (STATE) experiment at Poker Flat, Alaska. The studies by *Inhester et al.* [1990] and *Kelley et al.* [1990] during the Middle Atmosphere Campaign Summer in Northern Europe (MAC/SINE) campaign provided evidence of both isotropic and anisotropic turbulence. These observational studies suggest the intermittency of intense turbulent events. Radar observations can provide only a spatially and temporally averaged picture, whereas sporadic rocket observations may capture the full intensity of short-lived turbulent features, but only along the rocket trajectories.

Mesospheric temperatures and wind shears in our study are based on observations during the STATE campaign [*Kelley and Ulwick,* 1988; *Ulwick et al.,* 1988]. STATE investigated the phenomenon of polar mesospheric summer echoes (PMSE) (reviewed by *Cho and Kelley* [1993]). Our study is chosen to represent PMSE conditions, but the method is of more general applicability. The horizontal extent of the KH billows studied here (~3 km) is representative of noctilucent cloud billows that are observed at similar heights and times of year to those of PMSE.

Muschinski et al. [1999] applied numerical simulations of turbulence to the investigation of radar backscatter. They used a large-eddy simulation (LES) to simulate UHF wind profiler measurements in the convective boundary layer. The LES technique provided three-dimensional (3-D) simulated atmospheric variables in a procedure analogous to the DNS used in this study. For the study by *Muschinski et al.* [1999] the Bragg wavelength was within the inertial subrange of turbulence. For our mesospheric case we have the complication that the Bragg wavelength is comparable to the Kolmogorov microscale. For application to the mesosphere we include here electron and ion effects, and we present a procedure for calculating the Doppler spectral moments directly from the reflectivity distribution.

In this paper we simulate radar measurements of mesospheric turbulence and test the procedures used to infer turbulence parameters from radar data. The properties of the nondimensional, numerically simulated turbulent region are presented, along with a dimensionalization relevant to the mesosphere. Doppler VHF radar observations of the turbulent region are then simulated through direct calculation of the Dop-pler spectral moments from the reflectivity distribution and DNS velocities. The radar frequency of 50 MHz considered here is representative of typical VHF systems used in mesospheric observations and from which key turbulent parameters such as energy dissipation rates are estimated.

We address the following questions: (1) How do turbulent layers in the mesosphere affect VHF radar backscatter? (2) What information does radar back-scattered power provide about the turbulent layer? (3) How can we best interpret radar Doppler velocity? (4) Do local, instantaneous energy dissipation rates extracted from simulated VHF radar Doppler spectral widths agree with direct calculations from the local, instantaneous, 3-D velocity shears?

2. Simulation of Turbulence in the Mesosphere

2.1. Direct Numerical Simulation

The direct numerical simulation (DNS) of turbulence in a stratified shear environment presented by *Werne and Fritts* [1999] forms the basis of this study. The fluid dynamics equations were solved for an incompressible atmosphere with dimensionless flow variables: Reynolds number ($Re_{(t=0)} = 2000$), Prandtl number ($Pr = 1$), and Richardson number ($Ri_{(t=0,z=0)} = 0.05$). The simulation illustrates the evolution of a shear-initiated Kelvin–Helmholtz billow. An intense turbulent layer forms and gradually dissipates during the subsequent restratification of the fluid. A representative time sample ($t = 146$) was chosen in this study to characterize an intense turbulent layer. At this sample time the DNS provides three-component velocity and potential temperature at 720 streamwise, 240 spanwise, and 1440 vertical grid points. The simulation domain has dimensions $(4\pi,\ 4.2,\ 25)L$, where L is a unit length representing the half depth of the initial shear layer.

The initial potential temperature and streamwise velocity profiles are

$$\theta(t=0,z) = \beta z, \tag{1}$$

$$U(t=0,z) = U_0 \tanh(z/L), \tag{2}$$

where β is the potential temperature gradient, U_0 is the maximum velocity, and z is the height in the range [-12.5, 12.5]L. Choosing values for β, L, and U_0 is the basis for dimensionalization of the DNS.

Figure 1 presents three cross-sectional views of the DNS temperature perturbation field at t = 146 with a linear variation in gray scale shading. Note the well-mixed temperature field in the interior of the turbulent region and the strong vertical and horizontal temperature variations at the edges of the layer.

The primary advantage of using this simulation in the mesospheric applications is the presence of the inertial subrange of turbulence over approximately one decade or more [*Werne and Fritts,* 1999]. This is a significant improvement over earlier simulations of stratified shear turbulence which did not achieve an inertial subrange. Mesospheric KH billows are resolved at all scales by the simulation. The presence of an inertial range means that production and dissipation ranges are well separated such that we can calculate dissipation rates from velocity and temperature derivatives. The application of this nondimensional simulation to the mesosphere is detailed in section 2.2.

2.2. Dimensionalization to the Mesosphere

Because the DNS is a dimensionless calculation, it is necessary to scale the velocities and temperatures provided by the simulation to a mesospheric context. The dimensionalization presented here is based on observations carried out during the STATE campaign [*Kelley and Ulwick,* 1988; *Ulwick et al.,* 1988] and results in KH billow and turbulent layer dimensions representative of a range of mesospheric observations. It must be emphasized that the results presented in this paper are not critically dependent on the dimensionalization chosen. The real atmosphere supports a variety of turbulent structures. The dimensionalization provides a mesospheric test data set from which we simulate radar backscatter and examine the extraction of turbulent parameters.

The DNS streamwise dimension is initialized with an intense wind shear (68.5 m s^{-1} km^{-1}). Because the DNS uses periodic boundary conditions in the horizontal directions, the model domain is interpreted as a single billow in a larger region filled with a train of identical billows. The initial KH billow is centered at an altitude of 88.75 km. Values for the half depth of the initial shear layer L of 270 m and velocity scaling factor U_0 of 18.5 m s^{-1} were used, giving a spatial resolution in all three dimensions of 4.7 m between grid points. The full horizontal extent of the initial billow is $B = 4\pi L = 3.4$ km.

The Reynolds number determines the kinematic viscosity ν through

$$\nu = \frac{U_0 L}{Re}, \tag{3}$$

and therefore ν is 2.5 m^2 s^{-1}. Kinematic viscosity increases from $\sim$0.05 m^2 s^{-1} at 60 km to $\sim$1.5 m^2 s^{-1} at 85 km [*U.S. Committee on Extension to the Standard Atmosphere,* 1976]. *Lübken* [1992] gives a mesospheric viscosity value of 2.7 m^2 s^{-1} in the region 86.5–91.5 km obtained during the Noctilucent Cloud (NLC-91) rocket campaign. Hence our numerical viscosity value is appropriate for the upper mesosphere.

The temperature profile has been dimensionalized using a mean temperature $\theta_0 = 130$ K, representative of the cold summer mesopause. The initial potential temperature gradient β is related to velocity and length scales, the acceleration due to gravity ($g = 9.54$ m s^{-2} at mesospheric heights), and the Richardson number, by

$$\beta = \frac{Ri\theta_0}{g}\left(\frac{U_0}{L}\right)^2, \qquad (4)$$

resulting in a potential temperature gradient of 3.2 K km^{-1}.

The DNS does not resolve the full turbulence spectrum to the Bragg scale (3 m for 50 MHz radar). Figure 2 displays the one-dimensional potential temperature and velocity spectra calculated from the DNS at the time of this study. The inertial subrange of turbulence is indicated as the region satisfying the $k_x^{-5/3}$ power law. The Bragg wavenumber of 2094 km^{-1} is not reached by the DNS.

Figure 3 displays example horizontal and vertical velocity profiles at the time of the intense turbulent layer used in this study. Figure 4 displays the potential temperature profile through the center of the turbulent layer and the mean Brunt–Väisälä frequency profile calculated over the full horizontal simulation domain (720 x 240 elements). Height resolution in both Figures 3 and 4 is the DNS resolution of 4.7 m. We now proceed to use these dynamical variables to calculate dissipation rates, infer the VHF radar Doppler spectral moments, and investigate radar observations of mesospheric turbulence.

3. Results

3.1. Dissipation Rates

The DNS velocity structure, as summarized in Figure 3, is used to calculate energy dissipation rates ϵ from velocity shears $\partial \mathbf{V}/\partial \mathbf{x}$ through

$$\epsilon = \nu\left(\overline{\frac{\partial V_i \partial V_i}{\partial x_j \partial x_j}} + \overline{\frac{\partial V_i \partial V_j}{\partial x_j \partial x_i}}\right). \qquad (5)$$

Here ν is the DNS viscosity from (3), and averaging (denoted by the overbar) is performed over a cubic subvolume of 8^3 data points (dimensions (37.6 m)^3). Similarly, the thermal dissipation rate κ is calculated from the DNS potential temperatures θ through

$$\kappa = 2D\left(\overline{\frac{\partial \theta_i}{\partial x_i}}\right)^2, \qquad (6)$$

where D is the thermal diffusion coefficient ($D = \nu$ for $Pr = 1$ in the DNS).

Figures 5 and 6 illustrate the marked difference in vertical structure between energy and thermal dissipation rates. Clearly, the energy dissipates most strongly in the central region of the original billow, whereas thermal dissipation is greatest at the upper and lower edges of the turbulent region. This difference is caused by the different locations of the maximal gradients in the velocity and potential temperature fields (compare Figures 3 and 4a). Strong velocity fluctuations mix the thermal field most efficiently, reducing potential temperature gradients inside the turbulent layer. At both the upper and lower edges of the turbulent layer, strong potential temperature gradients persist, resulting in greater thermal dissipation.

3.2. Doppler Spectral Moments

The DNS provides a fine-resolution 3-D grid of potential temperature and three-component velocity. Doppler spectral moments relevant to mesospheric radar observations are now calculated from these fields. We use expressions from *Doviak and Zrnic* [1983, section 5.2, pp. 81–87]. Radar reflectivity values $\eta(x,y,z)$ are determined for cubic subvolumes of resolution (37.6 m)^3 (containing 8^3 data points) determined from the electron concentration spectrum [*Hill et al.*, 1999].

To investigate radar backscatter representative of PMSE conditions, we supplement the high-resolution DNS framework at the smallest scales by a subgrid-scale turbulence advection model described by *Hill and Mitton* [1998] and *Hill et al.* [1999]. This model determines the spectra and cospectra of temperature, ions, and electrons to the Bragg scale, given corresponding dissipation rates. This model is complicated because it involves multipolar plasma diffusion, which couples all ions and electrons by the multipolar electric field, and because the advection model is applicable for nonstationary turbulence and for coupling between the ionization and potential temperature fluctuations. Description of that model is beyond the scope of this paper. The model and its application to PMSE and to the STATE data are given by *Hill et al.* [1999], and further details are given by *Hill and Mitton* [1998].

For the results presented here, a three-ion formulation with a light positive ion was used (see *Hill et al.* [1999, Table 1] for three-ion model parameters). The model formulation has as many Schmidt numbers as there are species of ions. The largest ion Schmidt number in the PMSE model is 565, which ensures electron density fluctuations at the Bragg scale and causes agreement of the advection model with the rocket-measured electron density spectrum obtained from STATE [*Hill et al.,* 1999]. For application to VHF radar observations the dissipation rates were averaged on cubic subvolumes of 8^3 points, which is a cube 37.6 m on a side. Those averaged dissipation rates initialize the turbulence advection model, which calculates the electron density spectrum for that subvolume. The fact that 37.6 m is much larger than the Bragg wavelength (3 m) enables calculation of the reflectivity of the subvolume from the electron density spectrum evaluated at the Bragg wavenumber. This method is analogous to the method of *Muschinski et al.* [1999], who employ LES rather than DNS.

Radar backscattered power $P(z)$, the zeroth moment of the Doppler spectrum, is calculated from reflectivity $\eta(x,y,z)$ using

$$P(z) = \frac{\sum_{x,y} \eta(x,y,z) W(x,y,z)}{N_x N_y}. \qquad (7)$$

Doppler velocity $v_D(z)$, the first moment, is obtained from the radial velocity $v_R(x,y,z)$ using

$$v_D(z) = \frac{\sum_{x,y} v_R(x,y,z)\eta(x,y,z)W(x,y,z)}{P(z)N_xN_y}. \qquad (8)$$

The Doppler spectral width $\sigma(z)$, the second moment of the Doppler spectrum, is

$$\sigma^2(z) = \frac{\sum_{x,y} v_R(x,y,z)^2\eta(x,y,z)W(x,y,z)}{P(z)N_xN_y} - v_D^2(z). \qquad (9)$$

Here N_x and N_y are the numbers of scattering subvolumes in the streamwise and spanwise directions, respectively.

The averaging process is a key factor in the following discussion of the determination of turbulence parameters from actual radar observations. This calculation assumes no phase consistency between the individual scattering volumes, meaning that there is no Fresnel scattering included; this is discussed more fully by *Muschinski et al.* [1999].

$W(x,y,z)$ is the radar power weighting function [*Doviak and Zrnić,* 1983], which depends on the individual radar system. $W(x,y,z)$ here contains both a Gaussian range weighting function (half-power half width of 300 m) and an angular weighting function across the beam $I(\phi)$. Here we simulate measurements with a 50 MHz radar in the vertical mode with height resolution of 300 m and half-power beam width of 2.2°, based on the configuration used for turbulence observations with the Poker Flat radar [*Watkins et al.,* 1988]. The power weighting function across the vertical beam is (B. Balsley, private communication, 1999)

$$I(\phi) = \left(\frac{\sin\ [M\chi(\phi)]}{M\chi(\phi)}\right)^2, \qquad (10)$$

where $\chi(\phi)$ is given by [e.g., *Jordan and Balmain,* 1968]

$$\chi(\phi) = \frac{2\pi}{\lambda} d \cos\ (\phi). \qquad (11)$$

Here M is the number of antennas ($M = 32$), d is the antenna spacing ($d = 3.2$ m), λ is the radar wavelength, and ϕ is the angle across the beam [*Balsley et al.,* 1980]. Note that we transform the range and angular dependence into Cartesian coordinates for application to the gridded reflectivities.

The finite radar beam width results in "beam width broadening," which leads to a spurious increase in the observed Doppler spectral width [*Hocking,* 1983]. The relatively narrow beam width of the Poker Flat radar has been shown to require a negligible correction for beam width broadening [*Watkins et al.,* 1988].

Different radar pulse volumes mean larger or smaller averaging volumes for the returned power, as well as different weighting applied to the reflectivities. The DNS-based KH billow wavelength is 3.4 km compared with the horizontal extent of the Poker Flat radar pulse volume of ~2.5 km x 2.5 km at 88.75 km altitude. If this pulse volume is centered at the middle of the billow, then it resides within the computation domain. If we place the center of the pulse volume at or near the edge of the computation domain, then the portion of the pulse volume that is beyond the edge of the domain is within an adjacent billow, as necessitated by the periodic boundary conditions. When visualized in Figure 1, this means that the computation for the portion of the pulse volume beyond the domain is performed by wrapping that portion to the opposite side of the billow in Figure 1. In this study, the center of the radar pulse volume is on a vertical line through the middle of the DNS domain.

Figure 7

Figure 7 shows the vertical structure of the radar backscattered power $P(z)$ (equation (7)), which is strongly correlated with the vertical structure of the thermal dissipation rate (Figure 6). Figure 8 illustrates the mean Doppler velocity calculated using (8). Figure 9 shows $\sigma(z)$ from (9). These results are discussed in detail in sections 3.3.1–3.3.3.

Figure 8

Figure 9

3.3. Implications for Radar Observations

3.3.1. Radar backscattered power. The features of the simulated radar response to a turbulent structure are of vital importance in the interpretation of observations. In particular, Figure 7 shows that a single turbulent event in a stably stratified environment can produce two regions with strong temperature gradients and hence two peaks in reflectivity and backscattered power. Although this result is based on dimensionalization for a mesospheric case and the ion model for PMSE conditions of *Hill et al.* [1999], similar turbulent events will clearly drive analogous reflectivity variations in other parts of the atmosphere.

In light of these numerical results, we examine previous descriptions of radar observations of mesospheric turbulence. We note that there is insufficient information as yet to conclude that specific turbulent layers observed by VHF radar in the mesosphere are KH billow induced. Hence we focus on the vertical structure of the observed backscattered power at a late time in the turbulent evolution, where the generating instability has given way to a well-mixed central region surrounded by regions with strong temperature gradients. *Rastogi and Bowhill* [1976] concluded from radar autocorrelation functions that more than one turbulent layer existed within their ~5 km range resolution. In addition, they suggested discrete layers of turbulence with a separation of ~1 km. From our results we suggest that these observations are indicative of the upper and lower edges of a turbulent layer, but not multiple isolated turbulent layers. Further, the estimated layer separation of *Rastogi and Bowhill* [1976] suggests an approximate turbulent layer thickness, because the separation of peaks in the power profile (Figure 7) indicates that the power maximizes at the edges of a turbulent layer.

An estimate of layer thickness of $\sim$1 km is obviously a different interpretation of data from that of thin layers separated by $\sim$1 km. This estimate provides further support for larger vertical extents of KH billows in the mesosphere. *Rastogi and Bowhill* [1976] describe the narrowness of the turbulent layers, and this can now be seen to be suggestive of the narrow ($\sim$200 m half width) peaks in the power and reflectivity profiles (Figure 7).

In our simulation the initial shear layer half depth is specified as 270 m, which leads to a peak separation in the reflectivity profile of 1.2 km ($\sim 4L$). The height extent of the regions of large thermal dissipation is 1.7 km ($\sim 6L$). At different times in the simulation the detailed vertical structure of energy and thermal dissipation rates varies. Figure 4 of *Werne and Fritts* [1999] shows the evolution of the vertical structure of the temperature and Richardson number, which indicates that a double-peaked structure in the temperature gradients persists throughout much of the turbulent layer's evolution. Hence we expect that the double-peaked backscattered power profile would be a persistent feature of a VHF radar observation of a KH billow.

3.3.2. Doppler velocity. Figure 8 illustrates the calculated mean Doppler velocity v_D (equation (8)) and the mean vertical velocity from the DNS which has been weighted and averaged over the radar pulse volume. It must be noted that the mean vertical velocity would be zero when averaged over the full DNS volume (i.e., the full billow extent). The dashed line in Figure 8 indicates that much of the vertical structure evident in v_D results from the process of averaging and weighting over the radar pulse volume. Figure 8 has important implications for the interpretation of v_D. Strong local variations in reflectivity interact with strong variations in vertical velocity (e.g., Figure 3c) to produce a complex distribution of bright scatterers. In addition, the power weighting across the vertical beam $I(\phi)$ results in a stronger radar return from the central region of the pulse volume. Remnants of the initial KH billow velocity structure lead to an anisotropic velocity distribution (see Figure 1). Hence v_D is a "convolution" of reflectivity, vertical velocity, and beam weighting effects and is not a true vertical velocity under the nonuniform reflectivity conditions of this simulation.

The magnitude of the v_D bias shown in Figure 8, $\sim$1 m s^{-1}, is representative of that found in VHF radar observations [e.g., *Muschinski,* 1996]. We use the hydrodynamics convention of positive velocity indicating upward motion, which is opposite to the radar convention. The radar viewing angle and segment of the billow region imaged by radar will result in a range of velocity biases for a given KH billow structure. A further study is underway to investigate the occurrence of positive and negative biases. The concept of v_D representing an average vertical velocity over the radar pulse volume is challenged by this result, since v_D is not a straightforward spatial average of several scatterers of equal reflectivity. Instead, the reflectivity structure is nonuniform, and therefore the vertical structures of both vertical velocity and reflectivity are responsible for the calculated mean Doppler velocity. We anticipate further studies at later times in the turbulent evolution to investigate the v_D calculation more fully.

3.3.3. Spectral width and energy dissipation rate. Figure 9 shows vertical profiles of the horizontally averaged Doppler spectral width $\sigma(z)$ calculated from (9). In these calculations we have determined $\sigma(z)$ directly from the DNS velocities and the reflectivity. Analysis of experimental radar data requires calculation of the radial component of the RMS turbulent velocity v_{RMS}, which is related to the full width at half maximum of a Gaussian fit to the Doppler frequency spectrum $f_{1/2}$ through [*Hocking,* 1983]

$$v_{\mathrm{RMS}}(z) = \frac{\lambda}{2}\frac{f_{1/2}}{\sqrt{2\ln 2}}. \qquad (12)$$

The indirect (radar-like) calculation of energy dissipation rate is then normally expressed as [e.g., *Weinstock,* 1981; *Hocking,* 1996]

$$\epsilon_{\text{radar}} = C v_{\text{RMS}}^2 N, \tag{13}$$

where N is the Brunt–Väisälä frequency. For our DNS-based calculation, $v_{\text{RMS}} = \sigma(z)$ so that (13) can be used to estimate ϵ without applying (12).

The determination of ϵ_{radar} using (13) has several major sources of uncertainty. First, values for the constant C have ranged from 0.1 to 0.5, with two commonly used values of 0.4 and 0.47 [*Hocking,* 1983, 1996]. Here we use $C = 0.47$, consistent with *Hocking* [1996]. *Weinstock* [1981] obtained $C = 0.5$ from theoretical considerations. Second, the value of N is spatially and temporally variable, as well as highly dependent on the resolution of any temperature measurements available. Interpretation of N in a turbulent environment requires care. Finally, in radar data processing, a value of v_{RMS} must be calculated through (12). This means that v_{RMS} will depend on the fitting procedure used to estimate $f_{1/2}$.

The DNS approach allows a direct test of (13). A calculation of ϵ using (13) was carried out assuming a constant value of $N = 0.0134$ rad s^{-1}, which is the mean N across the turbulent region (dashed line in Figure 10). This is comparable to typical calculations from radar data where simultaneous temperature profiles are seldom available. In a second calculation, not shown, we used the high-resolution profile in Figure 4b to carry out a full calculation of (13), including the detailed vertical structures of both the turbulent velocities and N. The double-peaked structure in N shown in Figure 4b was found to result in ϵ profiles that did not reflect the actual DNS ϵ. *Hocking* [1996] has also suggested a correction factor, c_f, and in these calculations we have found a height-dependent correction factor.

Figure 10 compares energy dissipation rates calculated directly from the simulation and values determined from the Doppler spectral widths. The inclusion of the true variation in N across the turbulent layer leads to a very different vertical structure of energy dissipation rate than that expected from Figure 5. An average N in (13) results in vertical structure of the energy dissipation rate similar to the exact calculation. Therefore these results suggest that an average value of N provides an estimate of energy dissipation rates more in line with DNS-based calculations, within a factor of approximately 5, by means of (13).

4. Discussion

We have analyzed simulated VHF radar backscatter from a turbulent region which was generated through stratified shear instability using a direct numerical simulation (DNS) technique. Key insights provided by the numerical simulation were the fundamental differences between the vertical structure of energy and thermal dissipation rates (Figures 5 and 6). Energy dissipation rate was found to maximize in the central region of the turbulent layer at the time examined, whereas thermal dissipation was confined to the upper and lower boundaries of the turbulent region. These different structures are a consequence of the turbulent evolution that leads to an annihilation of temperature gradients in the central region, while velocity gradients remain strong [*Werne and Fritts,* 1999].

Backscattered power profiles were closely correlated with both N and thermal dissipation rate. These quantities exhibited a double-peak structure caused by strong thermal gradients at the edges of the simulated turbulent layer (Figures 4 and 7). In cases where the Bragg wavenumber is further in the dissipation range [e.g., *Rastogi and Bowhill,* 1976], the dependence on energy dissipation rate may be more pronounced. In this study, the radar backscattered power is strongly correlated with thermal dissipation rather than energy dissipation.

The first moment of the Doppler spectrum, or Doppler velocity, was heavily influenced by the nonuniform reflectivity structure and the power weighting function across the beam. We see that individual, bright scatterers are contributing to the Doppler velocity return. A bulk view in terms of volume scatter presupposes a uniform reflectivity structure and equal power weighting across the observed volume, in which case Doppler velocity will be equal to atmospheric vertical velocity; whereas a turbulent environment gives rise to strong reflectivity variations, and hence Doppler velocity will be weighted by the reflectivity structure.

The results of this simulation lead to the following caution: Doppler velocity measurements may not represent atmospheric vertical velocities if radar backscattered power is observed to have a highly nonuniform structure, indicating strongly varying reflectivity. Strong variations in reflectivity appear to arise naturally in such turbulent flows. The concept of averaging over a height region cannot improve the Doppler velocity estimate in such situations because reflectivity variations will bias estimates at a variety of scales.

The research presented here has provided a first opportunity to test, and potentially validate, the important assumptions used to estimate mesospheric turbulence statistics from VHF radar measurements. The energy dissipation rates for a simulated turbulent structure representative of those identified in the mesosphere were calculated through two independent processes. The extremely high spatial resolution of the 3-D DNS permits an exact calculation of dissipation rates from the simulated velocity fields. In addition, estimates of energy dissipation were determined from the Doppler spectral width using techniques suggested by *Weinstock* [1981] and *Hocking* [1996]. It was found that the Doppler spectral width profile was correlated with the energy dissipation rate profile. As a result, energy dissipation rates calculated from Doppler spectral width (equation (13)) were qualitatively similar to those calculated directly from the DNS (Figure 10). The absence of quantitative agreement suggests caution in the application of these equations. Further, the dependence of energy dissipation on Brunt–Väisälä frequency suggested by *Weinstock* [1981] is brought into question by the simulation results. Backscatter at different stages in the turbulent evolution will be analyzed in a future paper in order to generalize these results.

Recently, a new dual-radar approach to the estimation of energy dissipation rates has been proposed for use in the lower atmosphere (T. Van Zandt, private communication, 1999). Using simultaneous observations at two separate radar frequencies avoids many of the difficulties with the spectral width technique discussed here. However, the extension of this dual-radar technique to mesospheric applications requires knowledge of electron and ion densities that is lacking.

Extensions of the current work will include applications to VHF radar backscatter in the troposphere and stratosphere, applications to MF and UHF radar observations of PMSE through full-wave backscatter calculations, evaluation of backscatter implications throughout the temporal evolution of turbulent layers, and extension of these concepts to simulations of mesospheric gravity wave breaking.

5. Conclusions

From this simulation study of a mesospheric turbulent layer we have been able to draw a number of conclusions: (1) VHF radar backscattered power was shown to maximize in the edge regions of a turbulent feature and not at the center of the original billow structure. Maximum power was not indicative of maximum energy dissipation rate. (2) Nonuniform reflectivity structure and radar beam weighting were shown to cause disagreement between vertical velocity and Doppler velocity. (3) Doppler spectral width was correlated with the simulation's energy dissipation rate; however, existing procedures to calculate energy dissipation rates from Doppler spectral width did not result in quantitative agreement.

Acknowledgments. We thank K. A. Mitton and W. D. Otto for their expert programming, and we thank B. Balsley, W. Hocking, H.–L. Liu, A. Muschinski, and T. Van Zandt for useful comments. This work was supported by the National Science Foundation under grant ATM-9618004, the Air Force Office of Scientific Research under grant F49620-98-C-0029, and the Air Force Research Laboratory under grant F19628-98-C-0030.

References

Balsley, B. B., and K. S. Gage, The MST radar technique: Potential for middle atmospheric studies, *Pure Appl. Geophys.*, *118*, 452–493, 1980.

Balsley, B. B., W. L. Ecklund, D. A. Carter, and P. E. Johnston, The MST radar at Poker Flat, Alaska, *Radio Sci.*, *15*, 213–223, 1980.

Cho, J., and M. Kelley, Polar mesosphere summer radar echoes: Observations and current theories, *Rev. Geophys.*, *31*, 243–265, 1993.

Doviak, R. J., and D. S. Zrnić, *Doppler Radar and Weather Observations*, Academic, San Diego, Calif., 1983.

Fritts, D. C., J. R. Isler, G. E. Thomas, and Ø. Andreassen, Wave breaking signatures in noctilucent clouds, *Geophys. Res. Lett.*, *20*, 2039–2042, 1993.

Fritts, D. C., J. R. Isler, and Ø. Andreassen, Gravity wave breaking in two and three dimensions, 2, Three-dimensional evolution and instability structure, *J. Geophys. Res.*, *99*, 8109–8123, 1994.

Fritts, D. C., J. R. Isler, J. H. Hecht, R. L. Walterscheid, and Ø. Andreassen, Wave breaking signatures in sodium densities and OH nightglow, 2, Simulation of wave and instability structures, *J. Geophys. Res.*, *102*, 6669–6684, 1997.

Gage, K. S., J. L. Green, and T. E. Van Zandt, Use of Doppler radar for the measurements of atmospheric turbulence parameters from the intensity of clear-air echoes, *Radio Sci.*, *15*, 407–416, 1980.

Hecht, J. H., R. L. Walterscheid, D. C. Fritts, J. R. Isler, D. C. Senft, C. S. Gardner, and S. J. Franke, Wave breaking signatures in OH airglow and sodium densities and temperatures, 1, Airglow imaging, Na lidar, and MF radar observations, *J. Geophys. Res.*, *102*, 6655–6668, 1997.

Hill, R. J., and K. A. Mitton, Turbulence-induced ionization fluctuations in the lower ionosphere, *Tech. Rep. ERL 454-ETL 68*, NOAA Environ. Technol. Lab., Boulder, Colo., 1998.

Hill, R., D. Gibson-Wilde, J. Werne, and D. Fritts, Turbulence-induced fluctuations in ionization and application to PMSE, *Earth Planets Space*, *51*, 499–514, 1999.

Hocking, W. K., On the extraction of atmospheric turbulence parameters from radar backscatter Doppler spectra, I, Theory, *J. Atmos. Terr. Phys.*, *45*, 89–102, 1983.

Hocking, W. K., An assessment of the capabilities and limitations of radars in measurements of upper atmosphere turbulence, *Adv. Space Res.*, *17*(11), 37–47, 1996.

Inhester, B., J. C. Ulwick, J. Cho, M. C. Kelley, and G. Schmidt, Consistency of rocket and radar electron density observations: Implication about the anisotropy of mesospheric turbulence, *J. Atmos. Terr. Phys.*, *52*, 855–873, 1990.

Jordan, E. C., and K. G. Balmain, *Electromagnetic Waves and Radiating Systems*, 2nd ed., Prentice-Hall, Englewood Cliffs, N. J., 1968.

Kelley, M. C., and J. C. Ulwick, Large- and small-scale organization of electrons in the high-latitude mesosphere: Implications of the STATE data, *J. Geophys. Res.*, *93*, 7001–7008, 1988.

Kelley, M. C., J. C. Ulwick, J. Röttger, B. Inhester, T. Hall, and T. Blix, Intense turbulence in the polar mesosphere: Rocket and radar measurements, *J. Atmos. Terr. Phys.*, *52*, 875–891, 1990.

Liu, H.-L., P. B. Hays, and R. G. Roble, A numerical study of gravity wave breaking and impacts on turbulence and mean state, *J. Atmos. Sci.*, *56*, 2152–2177, 1999.

Lübken, F.-J., On the extraction of turbulent parameters from atmospheric density fluctuations, *J. Geophys. Res.*, *97*, 20,385–20,395, 1992.

Muschinski, A., Possible effect of Kelvin–Helmholtz instability on VHF radar observations of the mean vertical wind, *J. Appl. Meteorol.*, *35*, 2210–2217, 1996.

Muschinski, A., P. Sullivan, D. Wuertz, R. Hill, S. Cohn, D. Lenschow, and R. Doviak, First synthesis of wind–profiler signals on the basis of large–eddy simulation data, *Radio Sci.*, *34*, 1437–1459, 1999.

Rastogi, P. K., and S. A. Bowhill, Scattering of radio waves from the mesosphere, 2, Evidence for intermittent mesospheric turbulence, *J. Atmos. Terr. Phys.*, *38*, 449–462, 1976.

Røyrvik, O., VHF radar signals scattered from the equatorial mesosphere, *Radio Sci.*, *18*, 1325–1335, 1983.

Røyrvik, O., and L. G. Smith, Comparison of mesospheric VHF radar echoes and rocket probe electron concentration measurements, *J. Geophys. Res.*, *89*, 9014–9022, 1984.

Taylor, M. J., and M. A. Hapgood, On the origin of ripple-type structure in the OH nightglow emission, *Planet. Space Sci.*, *38*, 1421–1430, 1990.

Thomas, G. E., Mesospheric clouds and the physics of the mesopause region, *Rev. Geophys.*, *29*, 553–575, 1991.

Ulwick, J. C., K. D. Baker, M. C. Kelley, B. B. Balsley, and W. L. Ecklund, Comparison of simultaneous MST radar and electron density probe measurements during STATE, *J. Geophys. Res.*, *93*, 6989–7000, 1988.

U.S. Committee on Extension to the Standard Atmosphere, *U.S. Standard Atmosphere 1976*, U.S. Gov. Print. Off., Washington, D. C., 1976.

Watkins, B. J., C. R. Philbrick, and B. B. Balsley, Turbulence energy dissipation rates and inner scale sizes from rocket and radar data, *J. Geophys. Res.*, *93*, 7009–7104, 1988.

Weinstock, J., Energy dissipation rates of turbulence in the stable free atmosphere, *J. Atmos. Sci.*, *38*, 880–883, 1981.

Werne, J., and D. Fritts, Stratified shear turbulence: Evolution and statistics, *Geophys. Res. Lett.*, *26*, 439–442, 1999.

D. Fritts, D. Gibson-Wilde, and J. Werne, Colorado Research Associates, 3380 Mitchell Lane, Boulder, CO 80301. (dave@co-ra.com; dgibson@co-ra.com; werne@co-ra.com) R. Hill, Environmental Technology Laboratory, NOAA, Boulder, CO 80303. (rhill@etl.noaa.gov)

Received October 12, 1999; revised February 7, 2000; accepted February 23, 2000.

This preprint was prepared with AGU's LaTeX macros v5.01. File Doppler formatted April 4, 2000.

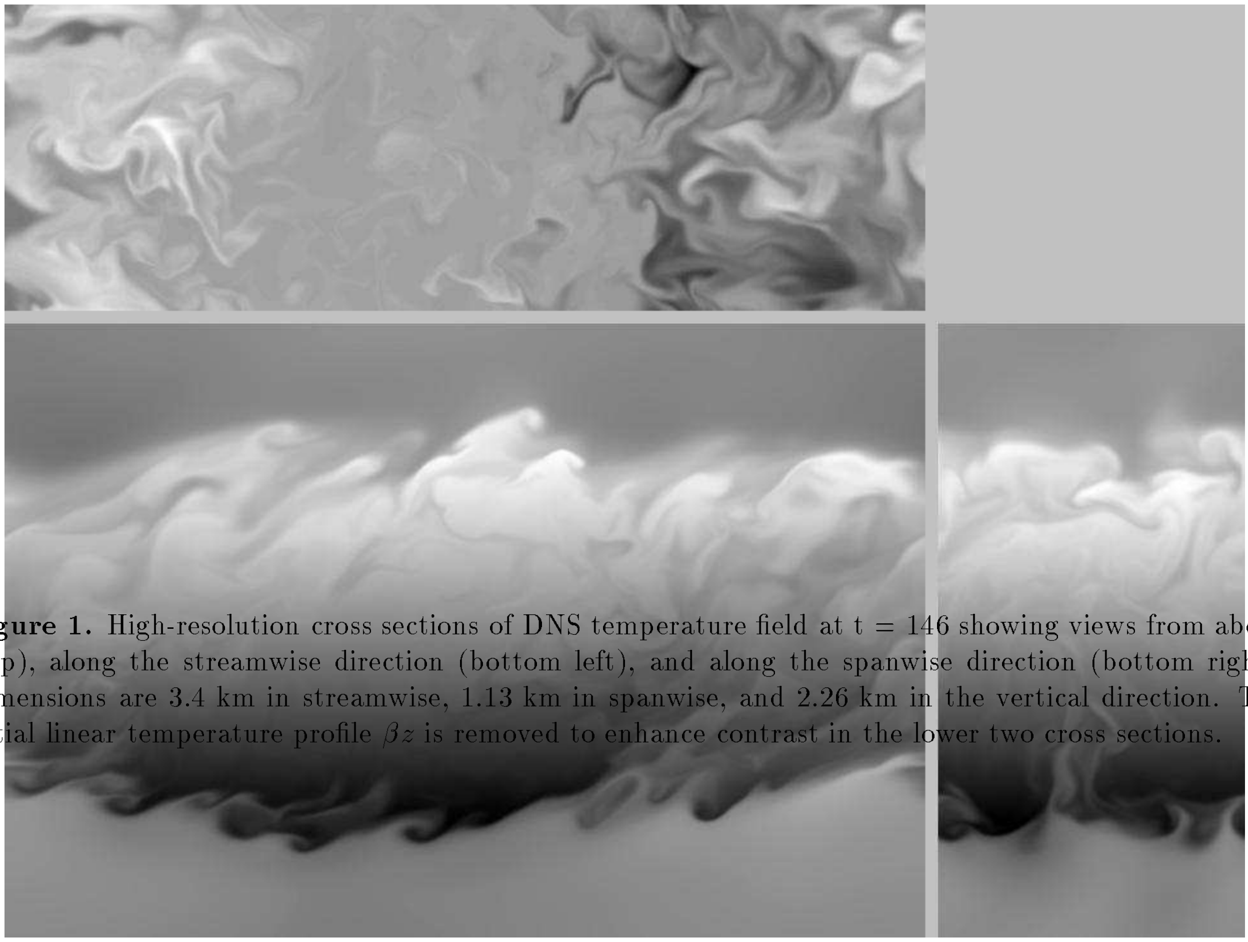

Figure 1. High-resolution cross sections of DNS temperature field at t = 146 showing views from above (top), along the streamwise direction (bottom left), and along the spanwise direction (bottom right). Dimensions are 3.4 km in streamwise, 1.13 km in spanwise, and 2.26 km in the vertical direction. The initial linear temperature profile βz is removed to enhance contrast in the lower two cross sections.

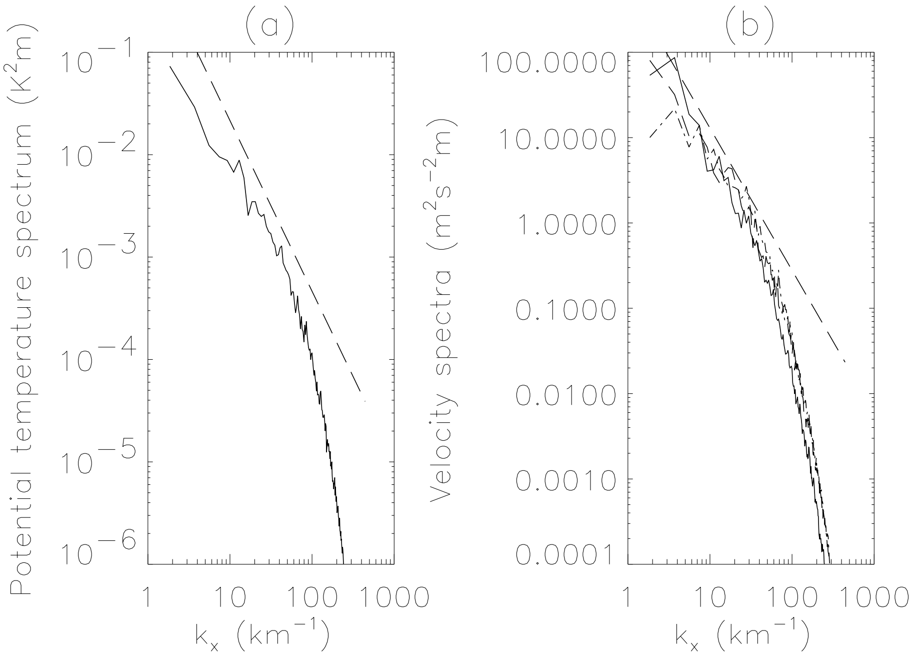

Figure 2. (a) Potential temperature spectrum (solid line) and (b) spectra of streamwise velocity (solid line), spanwise velocity (dash-dotted line), and vertical velocity (long-dashed line) from DNS. Dashed lines indicate the $\frac{-5}{3}$ power law.

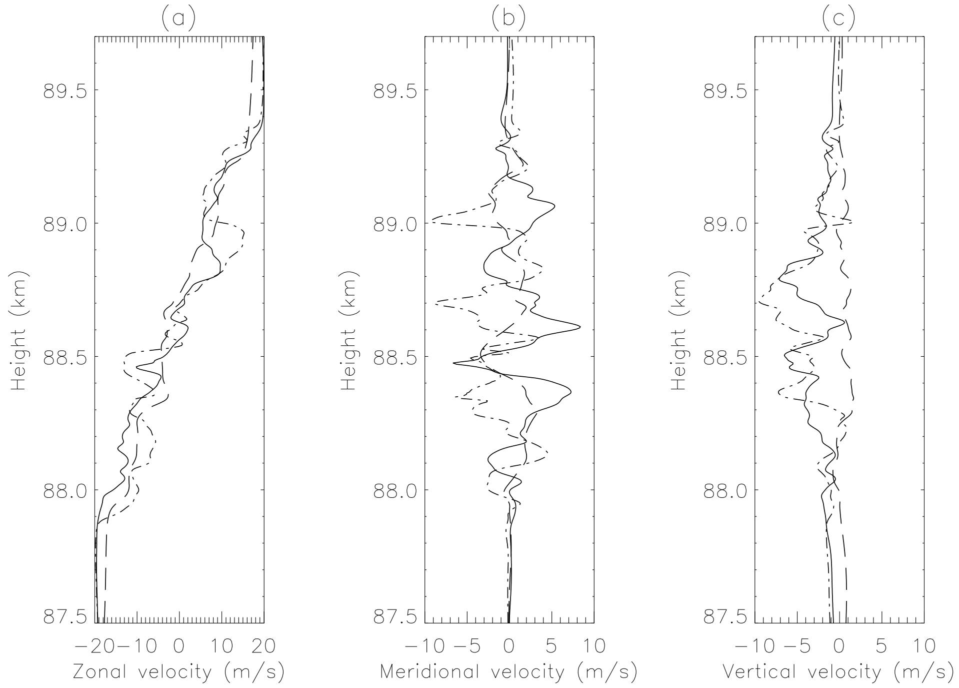

Figure 3. Profiles of (a) streamwise, (b) spanwise, and (c) vertical velocities dimensionalized to the mesosphere showing spatial variability of the velocity profiles. All profiles are at t = 146. Solid lines indicate profile through geometric center of turbulent region (where primary KH billow initially forms), dash-dotted lines indicate profile at the spanwise edge (streamwise center) of the domain, and the long-dashed lines indicate profile at the streamwise edge (spanwise center) of the domain.

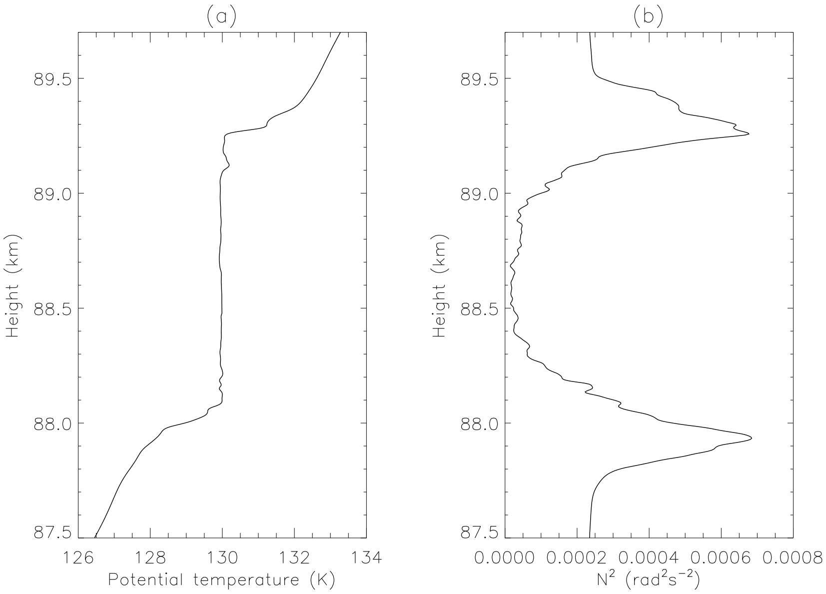

Figure 4. (a) High-resolution potential temperature profile through center of DNS domain. (b) Squared Brunt–Väisälä frequency averaged over the full horizontal extent of the KH billow.

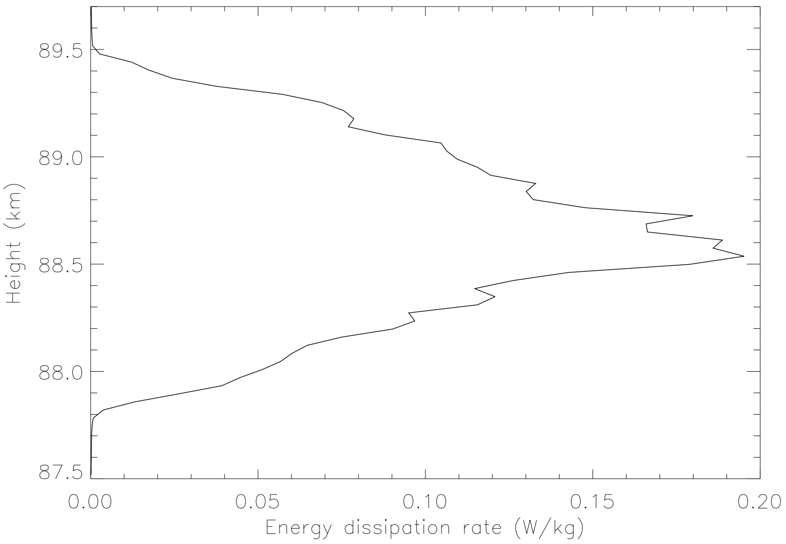

Figure 5. Energy dissipation rate ϵ calculated from the DNS and scaled to the mesosphere. Here ϵ is averaged over the central region of the billow domain.

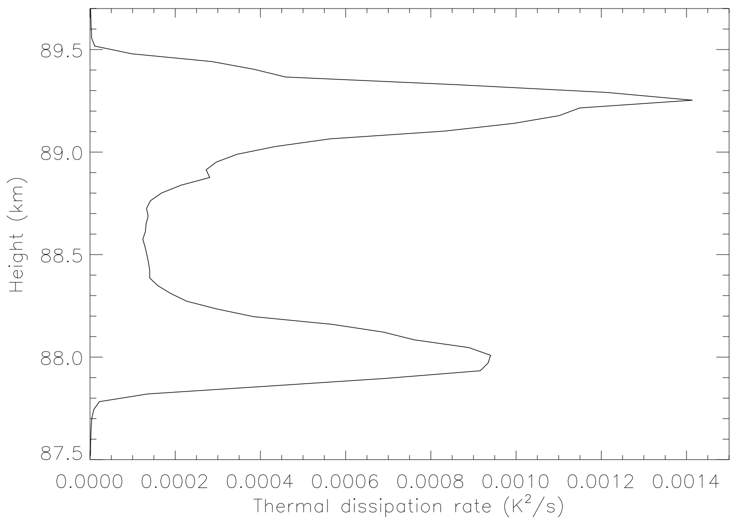

Figure 6. Thermal dissipation rate calculated from the DNS, presented as per Figure 5.

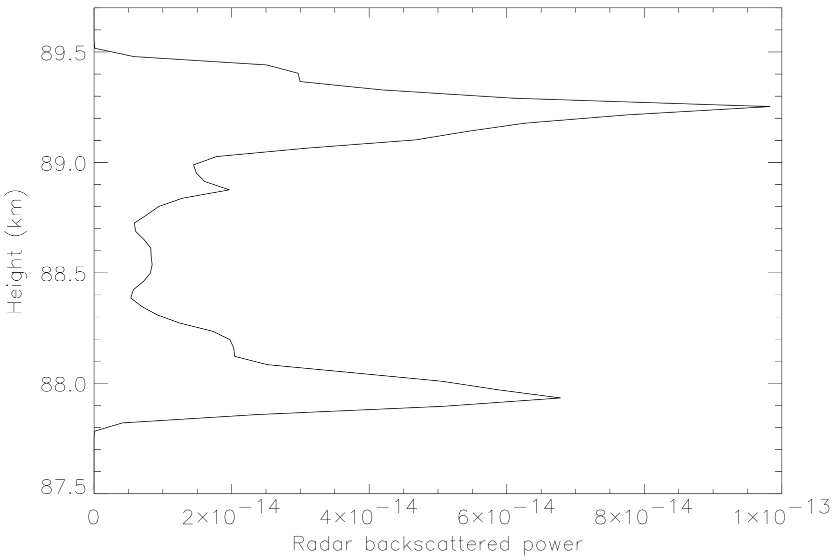

Figure 7. Simulated 50 MHz radar backscattered power $P(z)$ at 37.6 m vertical resolution averaged and weighted over radar-like pulse volume.

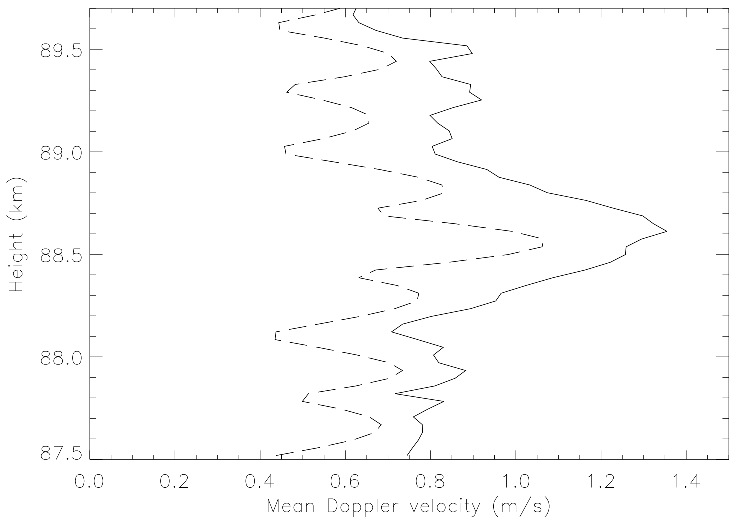

Figure 8. Solid line shows mean Doppler velocity profile at 37.6 m vertical resolution averaged and weighted over radar-like pulse volume. Dashed line is the vertical velocity (calculated using (8) with $\eta = 1$), averaged and weighted over radar-like pulse volume.

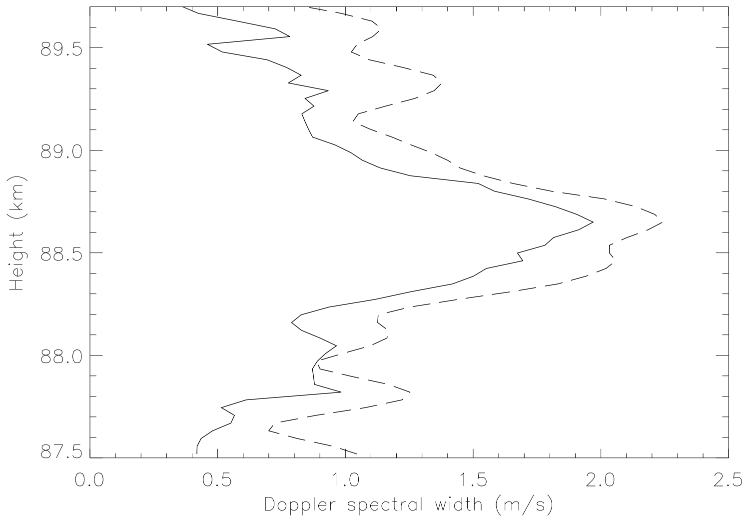

Figure 9. Doppler spectral width (solid line) presented as per Figure 8. Dashed line is the RMS velocity fluctuation calculated using (9) with $\eta = 1$.

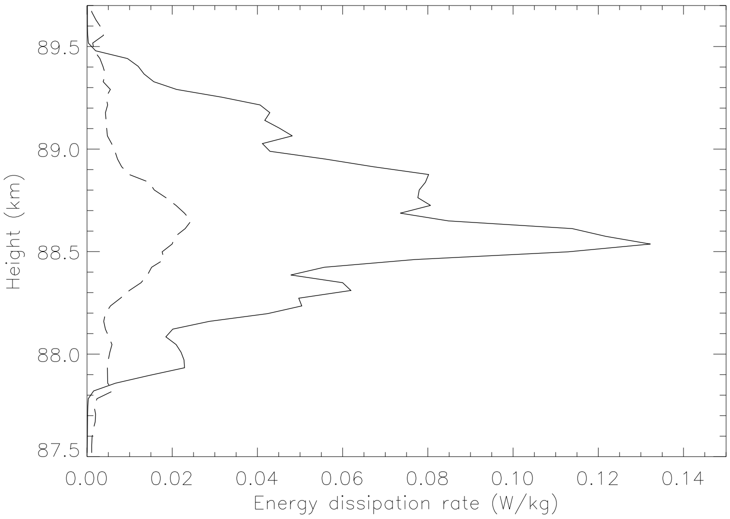

Figure 10. Comparison between DNS ϵ (solid line), averaged and weighted over the radar pulse volume, and $\epsilon_{\mathrm{radar}}$ with constant N (dashed line).